Publ. Astron. Soc. Japan (2014) 00(0), 1–10
doi: 10.1093/pasj/xxx000

arXiv:1611.06647v1 [astro-ph.HE] 21 Nov 2016

ATCA 16 cm Observation of CIZA J1358.9-4750: Implication of Merger Stage and Constraint on Non-Thermal Properties

Takuya AKAHORI[1*], Yuichi KATO[2], Kazuhiro NAKAZAWA[2], Takeaki OZAWA[1,3], Liyi GU[4], Motokazu TAKIZAWA[5], Yutaka FUJITA[6], Hiroyuki NAKANISHI[1], Nobuhiro OKABE[7,8], and Kazuo MAKISHIMA[2,9]

Received 2016 November 22; Accepted ⟨acception date⟩

Abstract

We report the Australia Telescope Compact Array 16 cm observation of a merging cluster, CIZA J1358.9-4750. Recent X-ray studies imply that this cluster is composed of binary clusters at an early stage of cluster merger. Using the EW367 configuration, we found no significant diffuse radio emission in and around the cluster. An upper limit of the total radio power at 1.4 GHz is $\sim 2 \times 10^{22}$ Watt/Hz in 30 square arcminutes which is comparable to a size of typical radio halos and relics. It is known that an empirical relation holds between the total radio power of radio relics and the X-ray luminosity of the host cluster in the late-stage of merger. The upper limit is about one order of magnitude below the flux expected from the relation, and suggests that the cluster is unlikely to be in a late stage of merger. Based on the assumption of energy equipartition, the upper limit gives the magnetic-field strength below $1.4\ (D/1\ \mathrm{Mpc})^{-1}(\gamma_{\min}/200)^{-1}\ \mu$G, where D is the depth of the shock wave along the sightline and $\gamma_{\min}$ is the lower cutoff Lorentz factor of the cosmic-ray electron energy distribution function.

Key words: galaxies: clusters: individual (CIZA J1358.9—4750) — intergalactic medium — shock waves — magnetic fields

1 Introduction

In the large-scale structure of the Universe, galaxy clusters can merge and convert its huge gravitational energy into thermal energy of the intracluster medium (ICM) (e.g. Sarazin 2002; Markevitch, Viklinin 2007). A collision sequence of two galaxy clusters can be divided into (i) the early stage where two clusters are getting close (e.g., Abell 399/401, Fujita et al. 2008), and (ii) the late stage where two clusters are receding from each other (e.g., Abell 3667, Nakazawa et al. 2009); any intermediate stage is short because of high-speed crossing of the two gravitational potential cores. Hydrodynamic simulations of merging galaxy clusters have shown that shock waves arise with position-dependent Mach numbers, M (e.g., Ryu et al. 2003; Takizawa 2008; Akahori & Yoshikawa 2010). In the early stage, shock waves with $M < 2$ arise in the linking region of the two clusters. Meanwhile, in the late stage, shock waves appear ahead of the two receding cores and are mostly on the collision axis. Stronger shocks with $2 < M < 4$ arise in the late stage because the shocks propagate toward cooler gas at cluster outskirts.

* Corresponding author: akahori@sci.kagoshima-u.ac.jp; [1]Graduate School of Science and Engineering, Kagoshima University, 1-21-35, Korimoto, Kagoshima, Kagoshima 890-0065, Japan; [2]Departure of Physics The University of Tokyo, 7-3-1 Hongo, Bunkyo-ku, Tokyo, 113-0033, Japan; [3]National Astronomical Observatory Japan, 2-21-1 Osawa, Mitaka, Tokyo 181-8588, Japan; [4]SRON Netherlands Institute for Space Research, Sorbonnelaan 2, 3584 CA Utrecht, the Netherlands [5]Department of Physics, Yamagata University, Kojirakawa-machi 1-4-12, Yamagata 990-8560, Japan [6]Department of Earth and Space Science, Graduate School of Science, Osaka University, Toyonaka, Osaka 560-0043, Japan [7]Department of Physical Science, Hiroshima University, 1-3-1, Kagamiyama, Higashi-Hiroshima, Hiroshima 739-8526, Japan [8]Hiroshima Astrophysical Science Center, Hiroshima University, Higashi-Hiroshima, Kagamiyama 1-3-1, 739-8526, Japan [9]MAXI Team, RIKEN, 2-1 Hirosawa, Wako, Saitama 351-0198, Japan

© 2014. Astronomical Society of Japan.

Identifying the merger stage, therefore, is the first step to understand physics in merging galaxy clusters. The merger stage has been investigated morphologically, from maps of X-ray surface brightness and optical weak-lensing mass (e.g., Okabe & Umetsu 2008; Okabe et al. 2011; Okabe et al. 2015). Another method is to see whether galaxy distribution is disturbed or cD galaxies are offset from X-ray peaks, which are frequently seen in the late stage (e.g., Abell 2163, Okabe et al. 2011). However, it has been rather difficult to conclude the merger stage through X-ray and/or optical observations alone; some clusters exhibit controversial substructures (e.g., RX J1347.5-1145, see Kitayama et al. 2016). The position of a shock wave and its Mach number are important evidence of the merger stage, but they can be studied only in a limited number of bright X-ray clusters (e.g., Finoguenov et al. 2010; Akamatsu & Kawahara 2013; Itahana et al. 2015).

Radio observation of diffuse synchrotron emission (e.g. Ozawa et al. 2015) provides a complementary tool to study shock waves and the merger stage. The emission suggests the presence of intergalactic magnetic field (IGMF) and cosmic-ray electrons (CRe). A short lifetime of GeV CRe, which emits synchrotron radiation in GHz bands, would mean that the emission is associated only with CRes which are recently accelerated (e.g., Sarazin 1986; Enßlin et al. 1998; Carilli & Taylor 2002). Observations in GHz bands have found several tens of radio relics (Feretti et al. 2012), whose unique, double-arc shapes have suggested the presence of shock waves and implied the late stage of their host merging clusters. Particle acceleration at merger shock waves has been studied mainly in terms of a model known as diffusive shock acceleration (DSA, e.g., Blandford & Eichler 1987; Kang & Ryu 2013; Vazza & Brüggen 2014). This theory can link the spectral index of radio emission with the Mach number of the shock.

It is known that a correlation holds between the total radio power, $P_{\rm f}$, and the X-ray luminosity, $L_{\rm X}$, of the host cluster. This $L_{\rm X}$–$P_{\rm f}$ relation applies to both radio halos and relics (e.g., Brunetti et al. 2007; Brunetti et al. 2009; Rudnick, Lemmerman 2009; Enßlin et al. 2011; Feretti et al. 2012; Xu et al. 2012; Govoni et al. 2013; Kale et al. 2015) and even to radio mini-halos in cool-core clusters (Gitti et al. 2015). Cassano et al. (2010) (see also Cassano et al. 2013) found that the majority of radio halos is observed in X-ray irregular clusters; this implies that radio halos as well as relics are related to cluster merger, and the stage of cluster merger thus affects the $L_{\rm X}$–$P_{\rm f}$ relation. While many late-stage clusters have been observed, there are only several candidates of early-stage clusters, and little is known about shock waves, radio emission, the radio spectral index, and the $L_{\rm X}$–$P_{\rm f}$ relation in the early stage (e.g. Akamatsu et al. 2016).

In the present paper, we report the first 16 cm (1–3 GHz) observations of CIZA J1358.9-4750 (hereafter CZ1359), which is a candidate of an early-stage merging clusters. The observations aimed to search diffuse radio emission. This paper is organized as follows. We describe the observations and data reduction in Sections 2 and 3, respectively. Results are shown in Section 4. Our discussion is presented in Sections 5, followed by concluding remarks in Section 6.

2 Radio Observations

2.1 The Target

CZ1359 is a nearby (redshift $z \sim 0.07$) galaxy cluster listed in the X-ray cluster catalog, CIZA (the Clusters in the Zone of Avoidance, Ebeling et al. 2002; Kocevski et al. 2007). This object exhibits two X-ray bright humps at South-East and North-West directions with a separation of $14' \sim 1.2$ Mpc. The humps are likely sub-clusters and the separation is ~ 0.7–0.8 times smaller than the virial radius (r_{200}, Kato et al. 2015) of each sub-cluster. Each X-ray core possesses a giant elliptical galaxy, which does not significantly deviate from the X-ray center. Kato et al. (2015) observed CZ1359 with the Suzaku X-ray telescope, and found that the ICM in the linking region between the cores is ~ 30 % hotter than that around the cores. Moreover, they discovered a temperature jump in the region and confirmed an associated brightness jump in an archival XMM-Newton X-ray image. The locations of giant elliptical galaxies and the X-ray temperature enhancement and jumps suggest that CZ1359 is in the early-stage, though further evidence is necessary to understand its thermal and dynamical states.

There are no scientific centimeter observations covering the CZ1359 field, except the 843 MHz SUMSS shallow survey[1]. There are also public data of the 150 MHz TGSS shallow survey[2]. SUMSS and TGSS detected several point sources but no diffuse radio emission. We refer to these data in our result.

2.2 The Observation

According to the numerical simulations (Akahori & Yoshikawa 2008; 2010; 2012), shock waves with $M \sim 1.5$ should appear in the linking region off the collision axis in the early stage, and $M \sim 3$ on the collision axis in the late stage. In fact, the former case (though with a somewhat smaller M) was confirmed in CZ1359, but our knowledge on this system is still limited. Therefore, considering the two possibilities as well as a possibility of existing radio halos, we observed the entire CZ1359 field which extends $\sim 30'$ in diameter.

The observation was made with the Australia Telescope Compact Array (ATCA). We adopted the 16 cm band (from

[1] Sydney University Molonglo Sky Survey; http://www.physics.usyd.edu.au/sifa/Main/SUMSS

[2] 150 MHz the Giant Metrewave Radio Telescope All-sky Radio Survey; http://tgss.ncra.tifr.res.in

Table 1. The observation log of CZ1359 with the ATCA.

pointing	right ascension	declination	date	period (UT)	frequency (MHz)	bandwidth (MHz)	exposure (min)
NE	13:59:10.0	-47:41:00.0	June 06, 2014	04:58 – 16:37	1100-3100	2048	560
NW	13:58:10.0	-47:40:00.0	June 08, 2014	05:02 – 17:06	1100-3100	2048	595
SE	13:59:10.0	-47:52:00.0	June 09, 2014	04:30 – 16:36	1100-3100	2048	595
SW	13:58:00.0	-47:51:00.0	June 10, 2014	04:31 – 16:46	1100-3100	2048	560

1.1 GHz to 3.1 GHz) which gives the widest field-of-view of $22'.3$ at the continuum center frequency 2.1 GHz. The survey required a trade-off between (i) an array configuration as compact as possible to gain a better sensitivity for diffuse emission, and (ii) a beam size of $\sim 1'$ or better so as to identify arc-shape structures of potential relics. We adopted the compromised, EW367 array configuration in which all six antennas were mounted in the east-west track. The minimum baseline was 46 m and the largest well-imaged structure at 2.1 GHz is $\sim 20'$ [3]. The maximum baseline was 367 m without the distant antenna 6 (CA06), and 4408 m with CA06. Resultant beam position angles and beam major/minor axes at 2.1 GHz were -89 ± 2 degree and $\sim 23'' \times 20''$ with CA06, and -1.6^{+7}_{-17} degree and $\sim 137'' \times 91''$ without CA06, respectively.

We adopted four pointings to cover the CZ1359 field. The ATCA observations were performed on June 6 (north-east, NE), June 8 (north-west, NW), June 9 (south-east, SE), and June 10 (south-west, SW) in 2014 (PI: T. Akahori, ID: C2916). Parameters of all pointings are listed in Table 1. Observation time for each pointing was 12 hours in total including overheads of standard calibration and antenna slew times. On-target exposure times were 9.33, 9.92, 9.92, and 9.33 hours in total for NE, NW, SE, and SW, respectively. These long trackings were provided with good hour angle coverage[4]. The system temperature was around 38 K (meridian passage) – 50 K (rising and setting) and those were stable during four observing days.

In each day, we observed the setup calibrator 0823-500 for 10 minutes at the start of the schedule, the band-pass calibrator 1934-638 (12.6 Jy at 2.1 GHz, a point source, no linear polarization) every 10 minutes at the middle and close of the schedule, and the gain/phase calibrator 1421-490 (7.38 Jy at 2.1 GHz, the distance from the target is 4.48 degree) for 3 minutes every 35 minutes of on-target observations. The 1M-0.5k Compact Array Broadband Backend (CABB, Wilson et al. 2011) receiver mode was selected to utilize the 2048 channels with 1 MHz spectral to allow full spectro-polarimetry observations.

[3] The largest well-imaged structure of 1-day observation is $\sim 230''$ at 6 cm with the 750 m configuration (section 1.7.1 of ATCA Users Guide, http://www.narrabri.atnf.csiro.au/observing/users_guide/html/atug.html). It scales $230'' * 2 * 16/6 \sim 20'$ at 16 cm with the 367 m configuration.

[4] The ATCA uses dual linear orthogonal feeds to measure two orthogonal linear polarizations simultaneously. The position angle of the polarization splitter is stationary with respect to the altra-azimutual-mounted antennas and so rotates on the sky.

3 Data Reduction

Data reduction was performed with the MIRIAD software version 1.5 following standard procedures. All data were loaded by the MIRIAD task ATLOD with options BIRBIE, RFIFLAG, XYCORR, and NOAUTO. Edge 40 channels (32 MHz bandwidth) which suffered from edge effects such as Gibbs phenomenon were removed by UVFLAG. Data were then split into subsets for the band-pass calibrator, the gain/phase calibrator, and the target, using UVSPLIT. For each subset, we performed UVFLAG, PGFLAG, and BLFLAG to flag out radio frequency interferences (RFIs). These were done iteratively until RFI signals disappear in visibility plots. The band-pass solution was made by MFCAL using the subset of the band-pass calibrator. The solution was transferred to the gain/phase calibration by GPCOPY, and then GPCAL was carried out to obtain the gain and phase solutions. The error of the absolute was computed by bootstrap estimation using GPBOOT. Finally, all solutions were applied to the target data using GPCOPY and GPAVER.

The visibility was transformed into real-space images with the MIRIAD task INVERT, where the robustness parameters, $r = 0.5$ and $r = 2.0$, were chosen to ensure the imaging quality for studies of compact sources and diffuse sources, respectively. We also created two different images; including and excluding CA06. The inclusion of these baselines improves the angular resolution, but the exclusion reduces a large uv gap and is commonly adopted for the study of diffuse emission. We performed standard multi-frequency CLEAN using the MIRIAD task MFCLEAN. For this purpose, images with three times wider field than the primary beam were prepared for the inversion with the MIRIAD task INVERT. The clean decomposition was carried out using MFCLEAN with a sufficiently-large number of iteration ($n_{\rm iter} = 5000$), and we searched for the number which minimize the rms on the cleaned image. We then retried MFCLEAN for the raw image with the best iteration number. In each frequency band, four pointing images were made and then they are linearly combined into a mosaic image by LINMOS. Stokes I, Q, and U data were reduced, but no significant signal and no meaningful image rms noise levels were obtained for Stokes Q and U in the CZ1359 field. Therefore, we only show the results of Stokes I below.

Since there is no previous 16 cm observation, we cannot directly calibrate our flux scale using previous observations. Instead, we have compared our result with the public SUMSS 843 MHz survey data. There is a bright point source SUMSS

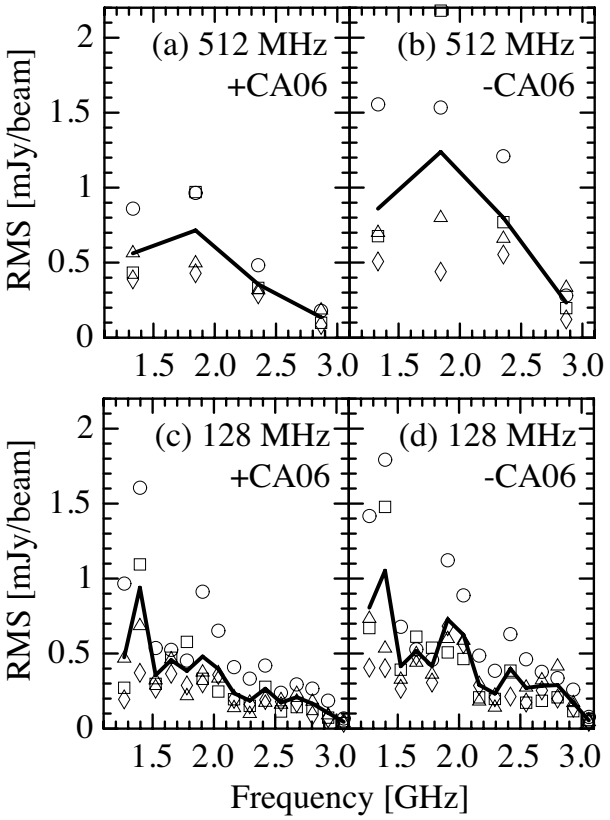

Fig. 1. (a) Image rms noise levels of NE (circles), NW (boxes), SE (triangles), and SW (diamonds) with 512 MHz simultaneous bandwidth. The solid line is the average for the four pointings. (b) The same as (a) but without CA06 baselines. (c)(d) The same as (a) and (b) respectively, but with 128 MHz simultaneous bandwidth.

J140033-473800 (14:00:33.5, -47:38:00). In our images with both $r = 2.0$ and $r = 0.5$, this source was detected with the peak flux of ~ 62.23 mJy at 1524 MHz and ~ 32.42 mJy at 2292 MHz, respectively. The corresponding spectral index

$$I_\nu \propto \nu^{-\alpha_{\rm obs}}, \quad (1)$$

(ν is the frequency) was $\alpha_{\rm obs} = 1.60$ which implied that this object was likely an unresolved Fanaroff-Riley radio galaxy rather than a quasar with a flat spectral index. If this is the case, it would be reasonable to assume that the index extends to the SUMSS band; the expected flux is ~ 160 mJy at 843 MHz. In comparison, the source flux is 130.6 mJy in the SUMSS catalog. Although the true spectral index is unknown, the flux scale of our observation is thus in agreement with that of the SUMSS within 23 %; this is acceptable for our study in this paper.

Images with the simultaneous bandwidths of 128 MHz and 512 MHz were made to compare the sensitivity levels. Here, in the former case we did not consider the bottom band (1140 MHz) and the top band (3060 MHz), since the sensitivities were low due to edge effects and RFIs. Figure 1 summarizes the sensitivity levels we have achieved with the robustness $r = 2.0$.

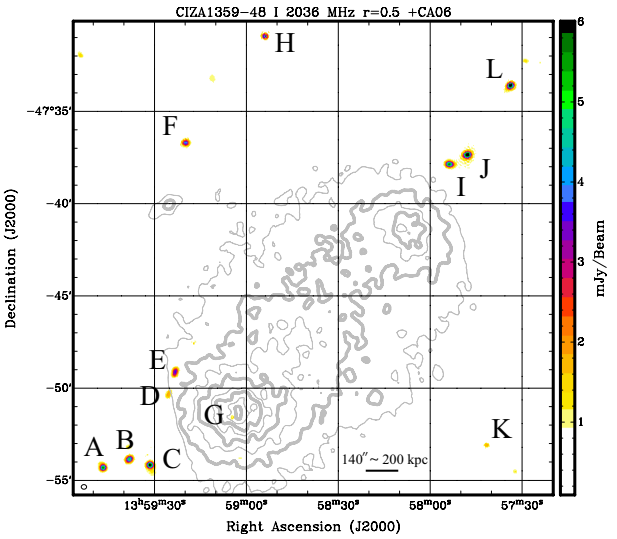

Fig. 2. Total intensity map of CZ1359 at 2036 MHz with CA06 baselines. Gray contours show the X-ray surface brightness (Kato et al. 2015).

Typical image rms noise levels were 0.5 mJy/beam (1.5–2 GHz) and 0.3 mJy/beam (2–3 GHz). They were several times worse than the theoretical noise level estimated with the exposure calculator provided by the observatory. This is thought to be mostly due to a very bright source PMN J1401-4733 (or SUMSS J140158-473336) located at the edge of each pointing image. The total intensity of this source, 0.433 Jy/beam at 1524 MHz, was ~ 1000 times higher than the image rms noise level, and this strong signal inevitably produces frequency-dependent sidelobes. Actually, the sidelobe effect makes the noise highest in the NE images, and increasing the simultaneous bandwidth above 128 MHz did not improve the image rms noise level, as shown in Fig. 1. The sidelobe effect cannot be removed by tuning the robustness and taper parameters in imaging, nor by iterating CLEAN algorithm.

4 Result

We first report the point sources detected in the CZ1359 field, and then study diffuse sources. As already mentioned, visibility data were imaged with the robustness $r = 0.5$ for point sources and $r = 2.0$ for diffuse sources to optimize each detection.

4.1 Point Sources

Radio point-like sources which have the flux larger than the detection limit ($> 5\sigma$) were explored, and twelve reliable point sources were found. Here, by eye, we rejected several spurious sources (not listed) which were unreliable in the sense that they appear only in some of band images and those positions shift in frequencies. Locations of the detected point sources are shown in Fig. 2 with alphabetic labels from East to West. Spectra of

Table 2. Summary of point sources in the CZ1359 field.

ID	Right ascension (error in arcsec)	Declination (error in arcsec)	This work† mJy/beam	$\alpha_{\rm obs}$	TGSS‡ mJy/beam	SUMSS* mJy/beam	2MASX
A	13:59:46.536 (1.139)	-47:54:14.37 (0.975)	6.90 ± 0.75	-0.22	18.32	13.2 ± 1.2	—
B	13:59:37.828 (1.342)	-47:53:52.25 (1.142)	6.38 ± 0.81	-1.09	16.16	—	—
C	13:59:31.085 (1.455)	-47:54:06.73 (1.239)	7.89 ± 1.08	0.56	21.76	—	Yes
D	13:59:24.841 (1.613)	-47:50:19.07 (1.431)	2.57 ± 0.39	-0.69	—	—	Yes
E	13:59:22.770 (1.625)	-47:49:05.25 (1.411)	4.75 ± 0.73	0.49	—	11.2 ± 1.1	Yes
F	13:59:19.316 (1.559)	-47:36:41.85 (1.344)	5.14 ± 0.76	-0.16	34.83	15.2 ± 1.1	—
G	13:59:03.488 (1.987)	-47:51:33.62 (1.709)	1.72 ± 0.33	0.22	—	—	Yes§
H	13:58:53.790 (1.151)	-47:30:55.74 (0.985)	4.91 ± 0.54	0.87	17.39	13.7 ± 1	—
I	13:57:53.588 (1.382)	-47:37:48.99 (1.186)	7.26 ± 0.95	-0.25	45.39	—	Yes
J	13:57:47.991 (1.508)	-47:37:19.39 (1.290)	9.17 ± 1.31	-0.06	44.29	26.4 ± 1.3	—
K	13:57:41.723 (0.975)	-47:53:03.78 (0.827)	2.12 ± 0.19	0.17	16.04	—	—
L	13:57:33.947 (1.271)	-47:33:33.36 (1.086)	8.21 ± 0.99	0.34	64.88	19.4 ± 1.1	—

†Flux at 2036 MHz. ‡Flux at 150 MHz. *Flux at 843 MHz. §See also the text.

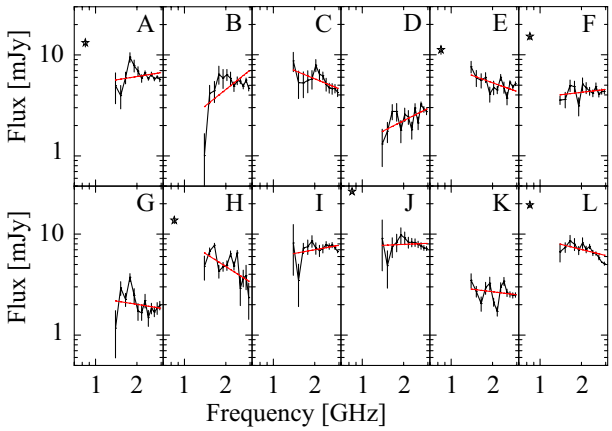

Fig. 3. Radio intensity spectra for twelve point-like sources in the CZ1359 field. Red lines are best-fits of the data. Stars indicates the data of SUMSS.

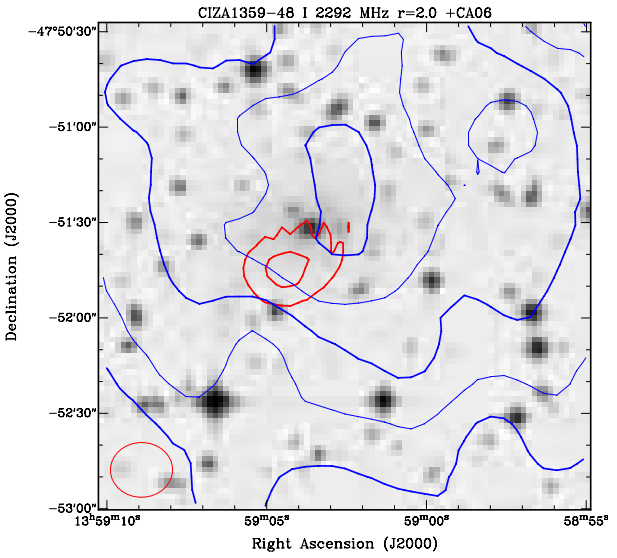

Fig. 4. The superposed image near the center of South-East sub-cluster of CZ1359. Background is the DSS optical image. Blue contours are the Suzaku X-ray surface brightness. Red contours are 2.3 GHz radio continuum images with levels of 1 (5.4 σ) and 2 (10.7 σ) mJy/beam. Also shown at the left-bottom is the beam size of the radio image.

these sources are shown in Fig. 3.

Table 2 summarizes the source coordinate and source peak flux, which were derived by using the MIRIAD task IMFIT with options OBJECT=POINT. Also listed is the spectral index which was obtained from the least square fit of the ATCA spectra with a simple power-law form (Eq. 1). We searched for possible association of objects using the NASA Extragalactic Database (NED), where the search range was set to be 30 arcsec in radius ($\sim 1.5 \times$ beam size). We also checked TGSS images to see possible counterpart emission in meter wavelengths. The results of association with flux densities of TGSS (150 MHz), SUMSS (843 MHz), and 2MASX (near-infrared) are listed in Table 2.

It is found that Source G, for which no SUMSS and TGSS counterparts exist, is located near the center of the SW cluster, 2XMM J135904.3-475125 (13:59:04.3, -47:51:25). A superposed map at 2292 MHz is shown in Fig. 4, where the coordinate errors of right ascension and declination are 1.419 arcsec and 1.226 arcsec, respectively, while the beam major and minor axes are 19.79 arcsec and 17.23 arcsec, respectively. The peak position of the radio emission deviates from that of the X-ray by about one beam size (~ 20 arcsec or ~ 30 kpc at $z = 0.07$). It also deviates from the central galaxy 2MASX J13590381-4751311 (13:59:03.8, -47:51:31) and a nearby galaxy 2MASX J13590223-4751502 (13:59:02.2, -47:51:50). The location implies that Source G is a radio lobe or a radio mini-halo, although its spectral index 0.22 is smaller than typical one. Otherwise, Source G is a point source, whose host galaxy is one of the two 2MASX sources or is too faint to list in the 2MASX catalog.

4.2 Diffuse Sources

The derived Stokes I images of CZ1359 at 2036 MHz with CA06 are shown in colors in Fig. 5(a), where gray contours

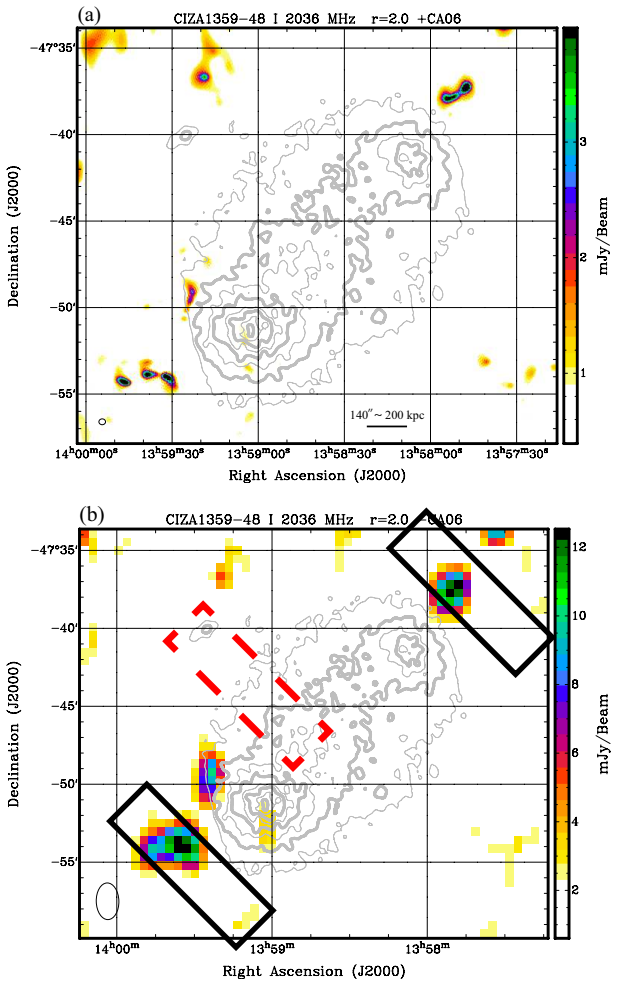

Fig. 5. Total intensity map of CZ1359 at 2036 MHz (a) with CA06 baselines and (b) without CA06 baselines. The color range is shown from 1 σ to 10 σ rms noise level. Gray contours show the X-ray surface brightness (Kato et al. 2015). The black-solid and red-dashed boxes indicate $10' \times 3'$ areas in which radio relics are expected in the late- and early-stage of cluster merger, respectively; the latter is associated with the observed X-ray shock front (Kato et al. 2015; section 5.4).

represent the X-ray surface brightness (Kato et al. 2015) for reference. We found only point sources, and did not detect diffuse radio emission in the field. The image without CA06 antenna baselines is also shown in Fig. 5(b). There are apparently extended emissions, but all of them are consistent with point sources convolved with a low-resolution beam, or noise. Note that the largest well-imaged structure at 2.1 GHz, $\sim 20'$, should be enough to detect possible diffuse emission in the CZ1359 field. We have examined all 128 MHz and 512 MHz bandwidth images we made, and found no diffuse emission any of them.

Let us consider a typical diffuse emission, i.e. radio halos and relics. They have a flux density 1 μJy/arcsec^2 at 1.4 GHz with $\alpha_{\rm obs} \sim 1$, and have similar surface brightness with each other (Feretti et al. 2012). Since the beam size without CA06 is 4539 arcsec^2 at 2.1 GHz, the expected surface brightness of this typical diffuse emission is 3.0 mJy/beam, or 10σ above the achieved sensitivity limit. Therefore, our non-detection firmly excludes the presence of typical diffuse emission in the CZ1359 field. For reference, the SUMSS with a beam size of 2295 arcsec^2 would detect such a radio source at 3.8 mJy/beam at 843 MHz, only $\sim 3\sigma$ above its sensitivity limit.

We derive the upper limit of radio power from the limit of surface brightness. This means that the radio power is proportional to an angular area of the emission; the radio power is broadly proportional to the square of the largest linear size (Feretti et al. 2012). A relatively large source is considered to gain a conservative upper limit. According to Feretti et al. (2012), radio halos and relics typically extend over a size several times larger than the cores of merging clusters. The expected angular size of radio emission in the CZ1359 field would be roughly 30 square arcminutes.

The expected total radio power can be given by

$$P = 4\pi D_{\rm L}^2 S_\nu \approx 1.2 \times 10^{22} I_\nu A \quad ({\rm Watt/Hz}), \tag{2}$$

where S_ν and I_ν are the flux and surface brightness, respectively, in units of mJy/beam, and A is the angular size of radio emission in beam. $D_{\rm L}(z = 0.07) \sim 9.74 \times 10^{26}$ cm is the luminosity distance for the cosmological parameters $H_0 = 70$ km s^{-1} Mpc^{-1}, $\Omega_{\rm M} = 0.3$, and $\Omega_\Lambda = 0.7$. The beam sizes at 1396 MHz are 955.9 arcsec^2 with CA06 and 29741 arcsec^2 without CA06. Considering the detection limit of $I_\nu = 0.5$ mJy/beam at 1.4 GHz and assuming the source angular size $A = 30$ arcmin^2, we obtain the upper limits $P = 6.75 \times 10^{23}$ Watt/Hz and $P = 2.25 \times 10^{22}$ Watt/Hz with and without CA06, respectively, for potential diffuse radio emission (radio halos, relics, and lobes) in the CZ1359 field.

Figure 6 shows the $L_{\rm X}$–$P_{\rm f}$ relation taken from Feretti et al. (2012). The arrow depicts the upper limit of CZ1359, $P_{\rm f} = 2.25 \times 10^{22}$ Watt/Hz, against the X-ray luminosity, $L_{\rm X} = 3.14 \times 10^{44}$ erg/s, derived from the Suzaku X-ray observation (Kato et al. 2015). Here, we derived the 0.1-2.4 keV luminosity from the bolometric luminosity in Kato et al. (2015), adopting the reported temperature and abundance, so as to compare with the other ROSAT data in Feretti et al. (2012). We summed up the X-ray luminosities of the two sub-clusters as the total X-ray luminosity of the system, following studies of other clusters.

The upper limit of CZ1359 falls by an order of magnitude below the $L_{\rm X}$–$P_{\rm f}$ relation. This observation first determined a strong upper limit of radio emission from CZ1359 in which the shock wave (with $M \sim 1.3$) is known in X-rays. To date, there are several observations which introduce similar upper limits of Mpc-scale radio emission with the radio power of $\lesssim 10^{23}$ Watt/Hz around the X-ray luminosity of $\sim 10^{44}$–10^{45} erg/s. The upper limit of CZ1359 is a factor of several below the limits obtained in previous works (not shown for clear display; see e.g. Kale et al. 2015).

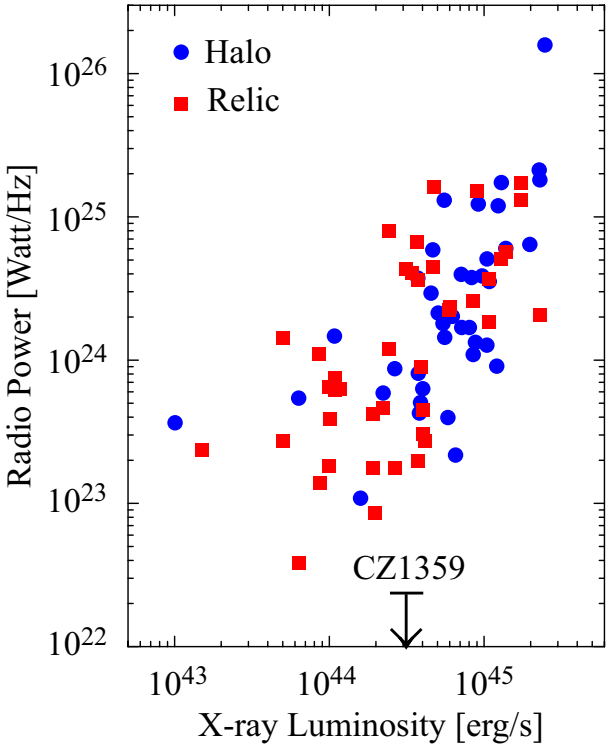

Fig. 6. The correlation between the radio power at 1.4 GHz and the 0.1 – 2.4 keV X-ray luminosity of 39 radio relics (red squares) and 41 radio halos (blue circles), all taken from Feretti et al. (2012). The black arrow indicates the upper limit of this work derived in Section 4.

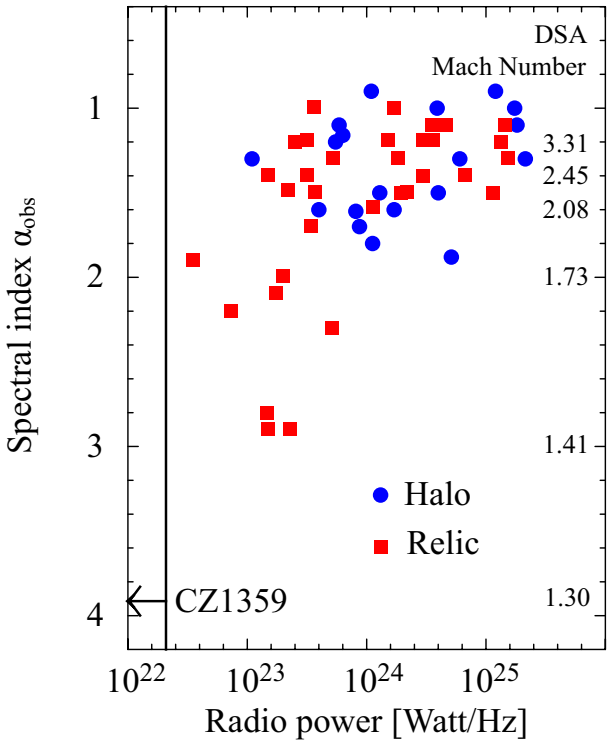

Fig. 7. The correlation between the radio power at 1.4 GHz and the spectral index $\alpha_{\rm int}$, all taken from Feretti et al. (2012). The black arrow indicates the constraint on CZ1359 from the present work (see text for details).

5 Discussion

The non-detection of radio halos/relics in this binary cluster may be ascribed to some reasons. One of the potential explanations would be the collision impact parameter and viewing angle, both of which can alter apparent morphology (e.g., Akahori & Yoshikawa 2010). While this geometrical dilution on radio halos and mini-halos are not well-known, the dilution on relics can be significant if the shock is not aligned to the line-of-sight (LOS). However, Kato et al. (2015) discussed bulk velocities of member galaxies and concluded that the collision is undergoing almost parallel to the sky plane. Therefore, the geometrical effect could be minor.

At the X-ray shock front, the expansion speed of the post-shock region is estimated to be 2400 km/s (Kato et al. 2015). Since apparent thickness of the shock region is $120''$ (168 kpc), the shock age is expected to be 68 Myr. This timescale is at least one order of magnitude shorter than the GeV electron cooling time (Sarazin 1999). Therefore, the underluminous radio emission is difficult to explain due to synchrotron cooling.

A more realistic explanation would be that CRes and/or magnetic fields are not yet established and hence synchrotron emission is too weak to be observed. In order to argue the possibilities, we discuss CRe content and magnetic-field strength below. Hereafter, we consider the shock acceleration of CRe.

5.1 Spectral Index – Radio Power Relation

The discussion starts with deriving the expected spectral index of radio emission. With the index of injected radio spectra, $\alpha_{\rm inj}$, the DSA model predicts the relation

$$\alpha_{\rm inj} = \frac{M^2+1}{M^2-1} - \frac{1}{2} \quad \text{or} \quad M^2 = \frac{2\alpha_{\rm inj}+3}{2\alpha_{\rm inj}-1}, \tag{3}$$

(e.g. Blandford & Eichler 1987) which links to the index of integrated radio spectra, $\alpha_{\rm obs}$, as

$$\alpha_{\rm obs} = \alpha_{\rm inj} + 0.5. \tag{4}$$

(see, e.g. Trasatti et al. 2015 references therein).

The $P_{\rm f} - \alpha_{\rm obs}$ relation for radio halos and relics taken from Feretti et al. (2012) is shown in Fig. 7. The majority of halos and relics have $\alpha_{\rm obs} < 2$, implying $M \gtrsim 2$ in the DSA picture. The arrow depicts $\alpha_{\rm obs} \sim 3.9$ based on the DSA with $M \sim 1.3$ given by the Suzaku X-ray observation. Our upper limit and the X-ray Mach number indicate that CZ1359 significantly deviates from the population of observed radio relics in the late stage and radio halos.

Figure 7 implies a weak positive correlation between the radio power and the spectral index, which is actually expected because both the radio power and the spectral index (the Mach number) may have a positive correlation with the energy of the merger event. If the trend is real, our upper limit expects a steep spectral index, which would be reasonable for the X-ray Mach

number of the early-stage shock but does not fit to $\alpha_{\rm obs} \sim 1.25$ for the $M \sim 3$ (mid-level of $M \sim 2-4$), i.e. does not fit to the late-stage shocks (Akahori & Yoshikawa 2010).

5.2 Cosmic-ray Electron Energy Distribution

The radio spectral index links to the CRe energy spectral index. We adopt a simple power-law form of the energy distribution (see Appendix). The standard formula of synchrotron radiation gives that the radio spectral index, $\alpha_{\rm inj}$, is related to the CRe energy spectral index, p, as

$$\alpha_{\rm inj} = \frac{p-1}{2}. \tag{5}$$

For the early-stage shock, $\alpha_{\rm obs} \sim 3.9$ derived from $M \sim 1.3$ means $p = 7.8$. Meanwhile, for the late-stage shocks, if we choose $\alpha_{\rm obs} = 1.5$ and $M = 2.24$ as a representative value of observed data in Fig. 7, we have $p = 3$.

In order to study the CRe density and total energy, we specify the range of the CRe energy spectral distribution. Here, energy loss can be significant at low and high energy regimes (Sarazin 1999) and p can be a variable. Since p is positive and steep in general, considering more energetic CRe does not significantly alter the estimation; the CRe density and energy changes only up to a few % as we vary the maximum energy $\gamma_{\rm max}$ from 3000 to infinity under the power-law form with $p \geq 3$. Meanwhile, the estimation depends significantly on the minimum energy $\gamma_{\rm min}$. It was studied that CRe with $\gamma \sim 300$ have the longest cooling timescale in a typical cluster environment and could be a dominant component (Sarazin 1999). Below, we adopt $200 \leq \gamma \leq 3000$ as a representative range.

5.3 Cosmic-ray Electrons and Magnetic Fields

CRe density and magnetic-field strength can be constrained simultaneously under the assumption that a radio emitter is in a simple minimum energy equipartition (see e.g., Pfrommer & Enßlin 2004). That is, the energy density of CRe, $\varepsilon_{\rm C}$, is equal to the energy of cosmic-ray ions, and is equal to a half of the energy density of magnetic field, ε_B, i.e. $2\varepsilon_{\rm C} = \varepsilon_B$. In this case, the cosmic-ray electron density N can be written as

$$N = N^*(p, \gamma_{\rm min}, \gamma_{\rm max}) B^2, \tag{6}$$

where N^* is the function of the energy spectral index p, and the energy range, $\gamma_{\rm min}$ and $\gamma_{\rm max}$ (see Appendix).

The synchrotron emissivity depends on the strength of magnetic field perpendicular to the LOS. We adopt a simple case where the strength of magnetic field perpendicular to the LOS is the same as that of magnetic field parallel to (the component parallel to the shock normal is neglected). It means $B = \sqrt{2} B_\perp$. The total radio intensity, I, can be written as

$$I = I^*(p, \gamma_{\rm min}, \gamma_{\rm max}) B^{(5+p)/2} \omega^{(1-p)/2}, \tag{7}$$

where $\omega = 2\pi\nu$.

The energy spectral index of $p = 7.8$ for the low Mach number shock gives almost negligible I and does not give a meaningful upper limit of CRe and magnetic field. Meanwhile, in the potential late-stage shocks, our upper limit, 0.5 mJy/beam, yields $B < 1.36$ μG ($200 \leq \gamma \leq 3000$) for $p = 3$ and the depth of the shock along the LOS, $D = 1$ Mpc. This upper limit is approximately proportional to $\gamma_{\rm min}^{-1}$ for $50 \leq \gamma_{\rm min} \leq 600$.

The upper limit of magnetic field translates into $N < 1.21 \times 10^{-10}$ cm^{-3}. Hence, the injected fraction of CR electrons $\xi_e = N/n < 1.21 \times 10^{-7}$ for the typical thermal electron density, 10^{-3} cm^{-3}. This is much below the acceleration efficiency discussed at the late-stage shocks, $\xi_e \sim 10^{-3}$–10^{-6} (see e.g., Kang & Ryu 2013; Vazza & Brüggen 2014). Thus, potential late-stage shock with $M \sim 2$ does not fit to the data. Also note that this upper limit is sensitivity limited, which means similar values are obtained for almost all area within the cluster.

5.4 Energy Budget

The thermal energy density, ε_T, and the magnetic energy density, ε_B, are respectively given in erg/cm^3 by

$$\varepsilon_T = \frac{3}{2} nkT = 4.00 \times 10^{-12} \left(\frac{n_{\rm e}}{10^{-3}\ {\rm cm}^{-3}} \right) \left(\frac{T_{\rm e}}{10^7\ {\rm K}} \right), \tag{8}$$

$$\varepsilon_B = \frac{B^2}{8\pi} = 3.98 \times 10^{-14} \left(\frac{B}{\mu{\rm G}} \right)^2, \tag{9}$$

where n and T are the ICM density and temperature, respectively, and $n_{\rm e}$ is the electron density. The ICM is assumed to be in thermal equilibrium ($T = T_{\rm e}$, $T_{\rm e}$ is the electron temperature) and fully-ionized with the mass fractions of Hydrogen $X = 0.76$ and Helium $Y = 0.24$. We can then estimate the energy budget of the nonthermal components under the energy equipartition, $\varepsilon_{NT} = 2\varepsilon_{\rm C} + \varepsilon_B = 2\varepsilon_B$;

$$\frac{\varepsilon_{NT}}{\varepsilon_T} < 1.99\ \% \left(\frac{B}{1\ \mu{\rm G}} \right)^2 \left(\frac{10^{-3}\ {\rm cm}^{-3}}{n_{\rm e}} \right) \left(\frac{10^7\ {\rm K}}{T_{\rm e}} \right). \tag{10}$$

As already described in Section 2.2, shock waves are expected to be present on the collision axis in the late stage, and the shocks would accompany radio relics. The potential radio relic regions with a size of $10' \times 3'$ are illustrated with the black solid boxes in Fig. 5(b). For the regions, the mean electron density is $n_{\rm e} \sim 0.5 \times 10^{-3}$ cm^{-3} and the temperature is $T_{\rm e} = 4.6 \times 10^7$ K (North) and $T_{\rm e} = 5.8 \times 10^7$ K (South) (Kato et al. 2015). Our limit of $B < 1.36$ μG thus gives rather loose upper limits, $\varepsilon_{NT}/\varepsilon_T < 16$ % and < 13 %, respectively.

Another $10' \times 3'$ potential radio relic region associated with the X-ray shock (Kato et al. 2015) is shown with the red dashed box in Fig. 5(b). For the region, $n_{\rm e} \sim 1.0 \times 10^{-3}$ cm^{-3} and $T_{\rm e} = 10.4 \times 10^7$ K, and our limit gives $\varepsilon_{NT}/\varepsilon_T < 3.5$ % beyond the DSA picture (i.e. $p = 3$). Because most of fresh CRe generated at the shock can survive for the shock age of 68 Myr, the derived energy fraction, < 3.5 % beyond the DSA picture, gives the

upper limit of the mean energy conversion rate, < 0.05 %/Myr, of thermal energy of the post shock gas. Another possibility is, of course, CRe has just start its acceleration and p is soft, so that the radio emission will be seen at low frequency and not in GHz band yet. Thus, low frequency radio observation will be important as the next step.

6 Concluding Remarks

We conducted the ATCA 16 cm observation of a merging galaxy cluster, CIZA J1358.9-4750 (CZ1359). We discovered a candidate of a radio galaxy, or a radio mini-halo, or a point source near the center of the South-East subcluster, but no diffuse radio sources. In the CZ1359 field, we obtained a significant upper limit of diffuse emission, which was about one order of magnitude below the one estimated using the X-ray luminosity – radio power relation for radio relics in the late-stage shocks and radio halos. It is therefore unlikely to consider that typical radio relics exist in CZ1359, and is difficult to consider CZ1359 as a late-stage merging cluster. Meanwhile, a scenario of the early-stage merger was not ruled out by our observation, as described later. Using the upper limit of total intensity and assuming a model of shock acceleration, we derived non-thermal properties at the X-ray shock front and potential shock fronts.

Assuming that the CZ1359 is in the early-stage of merger, the non-detection of diffuse radio emission at the X-ray shock front may be ascribed to the fact that the CRe energy spectrum is very steep under the DSA picture. This may be due to the fact that the X-ray shock is very young and the field amplification and particle acceleration are both in progress. It implies weak primordial magnetic field and less seed cosmic-ray electrons at the linking region of the cluster.

Recently, Fujita et al. (2015) and Fujita et al. (2016) proposed that the radio relics are produced through the second order Fermi acceleration, which is different from the DSA (the first order Fermi acceleration). If this is the case, electrons may not have had enough time to be accelerated, or scatterers of electrons (e.g. turbulence) may have not well developed behind the shock.

Finally, low frequency deep observation with MWA and GMRT would be important to further investigate possible diffuse radio emission in the CZ1359 field. In future, the Square Kilometre Array (SKA) and its precursors, ASKAP and MeerKAT, will provide an unprecedented sensitivity in Southern hemisphere (Johnston-Hollitt et al. 2015). They will advance the study of this cluster significantly.

This work was supported in part by JSPS KAKENHI Grant Numbers 26400218(MT), 15H03639(NK, TA), 15K05080(YF), 15K17614(TA), and by an University Research Support Grant from the National Astronomical Observatory of Japan (NAOJ). The Australia Telescope Compact Array is funded by the Commonwealth of Australia for operation as a National Facility managed by CSIRO.

Appendix. Synchrotron Radiation from Cosmic-Ray Electrons

Near a shock front, there are fresh CRe whose distribution can be represented as a simple power law with a constant spectral index p. The number density of CRe between the Lorentz factor γ and $\gamma + d\gamma$ is defined as

$$N(\gamma)d\gamma = N_0\gamma^{-p}d\gamma, \tag{A1}$$

where N_0 is the normalization in units of cm^{-3}. Therefore, the CRe number density is given by integrating the CRe energy density spectrum as

$$\begin{aligned} N &= N_0 \int_{\gamma_{\min}}^{\gamma_{\max}} \gamma^{-p} d\gamma \\ &= N_0 N_1(p, \gamma_{\min}, \gamma_{\max}) \quad (\mathrm{cm}^{-3}) \end{aligned} \tag{A2}$$

where $N_1 = [\gamma^{1-p}]_{\gamma_{\min}}^{\gamma_{\max}}/(1-p)$ ($p \neq 1$). Likewise, with the electron rest mass m_{e} and the speed of light c, the energy density of CRe can be calculated as

$$\begin{aligned} \varepsilon_{\mathrm{C}} &= N_0 m_{\mathrm{e}} c^2 \int_{\gamma_{\min}}^{\gamma_{\max}} \gamma^{1-p} d\gamma \\ &= N_0 m_{\mathrm{e}} c^2 N_2(p, \gamma_{\min}, \gamma_{\max}) \quad (\mathrm{erg/cm}^3) \end{aligned} \tag{A3}$$

where $N_2 = [\gamma^{2-p}]_{\gamma_{\min}}^{\gamma_{\max}}/(2-p)$ ($p \neq 2$). From the energy equipartition $2\varepsilon_{\mathrm{C}} = \varepsilon_B = B^2/(8\pi)$, we obtain the following relation

$$N_0 = \frac{B^2}{16\pi m_{\mathrm{e}} c^2 N_2}, \tag{A4}$$

where $N_0 \sim 1.0 \times 10^{-5}$ cm^{-3} for $200 \leq \gamma \leq 3000$ and $p = 3$. Eq.(A2) is written as

$$\begin{aligned} N &= N^*(p, \gamma_{\min}, \gamma_{\max}) B^2 \\ &= \frac{N_1 B^2}{16\pi m_{\mathrm{e}} c^2 N_2} \end{aligned} \tag{A5}$$

Specific Stokes parameters of synchrotron radiation from the electron population can be written as (see Rybicki & Lightman 1979; Waelkens et al. 2009),

$$I = \int G_1(p) N_0(r) B_\perp(r)^{(1+p)/2} \omega^{(1-p)/2} dr, \tag{A6}$$

$$Q + iU = \int G_2(p) N_0(r) B_\perp(r)^{(1+p)/2} \omega^{(1-p)/2} e^{2i\chi(r)} dr, \tag{A7}$$

where $B_\perp$ is the magnetic field perpendicular to the LOS, χ is the initial polarization angle at r, and $\omega = 2\pi\nu$ is the angular frequency. Other physical coefficients are $G_1(p) = 2g_1(p)j(p)$, $G_2(p) = 2g_2(p)j(p)$,

$$j(p) = \frac{1}{4\pi} \frac{\sqrt{3} q^3}{8\pi m_{\mathrm{e}} c^2} \left(\frac{2 m_{\mathrm{e}} c}{3q} \right)^{(1-p)/2}, \tag{A8}$$

$$g_1(p) = \frac{1}{1+p} 2^{(1+p)/2} \Gamma\left(\frac{p}{4} - \frac{1}{12}\right) \Gamma\left(\frac{p}{4} + \frac{19}{12}\right), \quad \text{(A9)}$$

$$g_2(p) = 2^{(p-3)/2} \Gamma\left(\frac{p}{4} - \frac{1}{12}\right) \Gamma\left(\frac{p}{4} + \frac{7}{12}\right), \quad \text{(A10)}$$

where, q is the electric charge and Γ is the Γ function. For a uniform medium with the depth D, Eq. (A6) is integrated as

$$I = \frac{G_1 D}{16\pi m_e c^2 N_2} B_\perp^{(1+p)/2} B^2 \omega^{(1-p)/2}. \quad \text{(A11)}$$

For a simple case where the strength of magnetic field perpendicular to the LOS is the same as that of magnetic field parallel to the LOS, $B = \sqrt{2} B_\perp$, the intensity is written as

$$\begin{aligned} I &= I^*(p, \gamma_{\min}, \gamma_{\max}) B^{(5+p)/2} \omega^{(1-p)/2} \\ &= \frac{2^{-(1+p)/4} G_1 D}{16\pi m_e c^2 N_2} B^{(5+p)/2} \omega^{(1-p)/2}. \end{aligned} \quad \text{(A12)}$$

References

Akahori, T., Yoshikawa, K. 2008, PASJ, 60, L19

Akahori, T., Yoshikawa, K. 2010, PASJ, 62, 335

Akahori, T., Yoshikawa, K. 2012, PASJ, 64, 12

Akamatsu, H., & Kawahara, H. 2013, PASJ, 65, 16

Akamatsu, H., Gu, L., Shimwell, T. W., Mernier, F., Mao, J., Urdampilleta, I., de Plaa, J.,& Röttgering, H. J. A. 2016, A&A, 593, L7

Blandford, R., & Eichler, D. 1987, Phys. Rep., 154, 1

Brunetti, G., Venturi, T., Dallacasa., D., et al. 2007, ApJL, 670, L5

Brunetti, G., Cassano, R., Dolag, K., & Setti, G., 2009, A&A, 507, 661

Carilli, C. L., & Taylor, G. B. 2002, ARA&A, 40, 319

Cassano, R., Ettori, S., Giacintucci, S., et al. 2010, ApJL, 721, L82

Cassano, R., Ettori, S., Brunetti, G., Giacintucci, S., Pratt, G. W., Venturi, T., Kale, R., Dolag, K., & Markevitch, M. 2013, ApJ, 777, 141

Ebeling, H., Mullis, C. R, & Tully, R. B. 2002, ApJ, 580, 774

Enßlin, T. A., Biermann, P. L., Klein, U., & Kohle, S. 1998, A&A, 332, 395

Enßlin, T., Pfrommer, C., Miniati, F., & Subramanian, K. 2011, A&A, 527, A99

Feretti, L., et al. 2012, A&A Review, 20, 54

Finoguenov, A., Sarazin, C. L., Nakazawa, K., Wik, D. R., & Clarke, T. E., 2010, ApJ, 715, 1143

Fujita, Y., et al. 2008, PASJ, 60, S343

Fujita, Y., Takizawa, M., Yamazaki, R., Akamatsu, H., & Ohno, H. 2015, ApJ, 815, 116

Fujita, Y., Akamatsu, H., & Kimura, S. S. 2016, PASJ, 68, 34

Gitti, M., Tozzi, P., Brunetti, G., et al. 2015, aska.conf, 76

Govoni, F., Murgia, M., Xu, H., Li, H., Norman, M. L., Feretti, L., Giovannini, G., & Vacca, V. 2013, A&A, 554, 102

Itahana, M., Takizawa, M., Akamatsu, H., et al. 2015, PASJ, 67, 113

Johnston-Hollitt, M., Govoni, F., Beck, R., et al. 2015, in Proc. of Advancing Astrophysics with the Square Kilometre Array (Trieste: SISSA), PoS (AASKA14)092, id.92

Kang, H., & Ryu, D. 2013, ApJ, 764:95

Kale, R., Venturi, T., Giacintucci, S., Dallacasa, D., Cassano, R., Brunetti, G., Cuciti, V., Macario, G., & Athreya, R. 2015, A&A, 579, A92

Kato, Y., Nakazawa, K., et al. 2015, PASJ, 67, 71

Kitayama, T., Ueda, S., Takakuwa, T., et al. (2016), PASJ, 68, 88

Kocevski, D. D., Ebeling, H., Mullis, C. R., & Tully, R. B. 2007, ApJ, 662, 224

Markevitch, M., & Vikhlinin, A. 2007, Physics Reports, 443, 1

Nakazawa, K. et al. 2009, PASJ, 61, 339

Okabe, N., & Umetsu, K. 2008, PASJ, 60, 345

Okabe, N., Bourdin, H., Mazzotta, P., & Maurogordato, S. 2011, ApJ, 741, 116

Okabe, N., Akamatsu, H., Kakuwa, J., Fujita, Y., Zhang, Y., Tanaka, M., & Umetsu, K. 2015, PASJ, 67, 114

Ozawa, T., Nakanishi, H., Akahori, T., Anraku, K., Takizawa, M., Takahashi, I., Onodera, S., Tsuda, Y., & Sofue, Y. 2015, PASJ, 67, 110

Prfommer, C., & Enßlin, T. A. 2004, MNRAS, 352, 76

Rudnick, L., & Lemmerman, J. 2009, ApJ, 697, 1341

Rybicki, G. B., & Lightman, A. P. 1979, Radiation processes in astrophysics (New York: Wiley-Interscience)

Ryu, D., Kang, H., Hallman, E., & Jones, T. W. 2003, ApJ, 593, 599

Sarazin, C. L. 1986, Reviews of Modern Physics, 58, 1

Sarazin, C. L. 1999, ApJ, 520, 529

Sarazin, C. L. (2002), ASSL, 272, 1

Takizawa, M. 2008, ApJ, 687, 951

Trasatti, M., Akamatsu, H., Lovisari, L., Klein, U., Bonafede, A., Brüggen, M., Dallacasa, D., & Clarke, Tracy. 2015, A&A, 575, 45

Vazza, F., & Brüggen, M. 2014, MNRAS, 437, 2291

Waelkens, A., Jaffe, T., Reinecke, M., Kitaura, F. S., & Enßlin, T. A., 2009, A&A, 495, 697

Wilson, E., et al. 2011, MNRAS, 416, 832

Xu, H., Govoni, F., Murgia, M., Li, H., Collins, D. C., Norman, M. L., Cen, R., Feretti, L., & Giovannini, G. 2012, ApJ, 759, 40